Title

Molecular-Scale Insights into the Heterogeneous Interactions between an m-Terphenyl Isocyanide Ligand and Noble Metal Nanoparticles.

Authors

Bi, Liya

Wang, Yufei

Wang, Zhe

et al.

Publication Date

2025-01-23

DOI

10.1021/acs.nanolett.4c05885

Peer reviewed

NANO LETTERS

pubs.acs.org/NanoLett
Letter

Molecular-Scale Insights into the Heterogeneous Interactions between an *m*-Terphenyl Isocyanide Ligand and Noble Metal Nanoparticles

Liya Bi,[#] Yufei Wang,[#] Zhe Wang,[#] Alexandria Do, Alexander Fuqua, Krista P. Balto, Yanning Zhang, Joshua S. Figueroa, Tod A. Pascal, Andrea R. Tao,[*] and Shaowei Li[*]

Cite This: *Nano Lett.* 2025, 25, 2027−2033

Read Online

ACCESS | Metrics & More | Article Recommendations | Supporting Information

ABSTRACT: The structural and chemical properties of metal nanoparticles are often dictated by their interactions with molecular ligand shells. These interactions are highly material-specific and can vary significantly even among elements within the same group or materials with similar crystal structure. In this study, we surveyed the heterogeneous interactions between an *m*-terphenyl isocyanide ligand and Au and Ag nanoparticles (NPs) at the single-molecule limit. Specifically, we found that the ligation behavior with this molecule differs significantly between that of Au and AgNPs. Surface-enhanced Raman spectroscopy measurements revealed unique enhancement factors for two molecular vibrational modes between two metal surfaces, indicating different ligand binding geometries. Molecular-level characterization using scanning tunneling microscopy allowed us to directly visualize these variations between Ag and Au surfaces, which we assign as two distinct binding mechanisms. This molecular-scale visualization provides clear insights into the different ligand−metal interactions as well as the chemical behavior and spectroscopic characteristics of isocyanide-functionalized NPs.

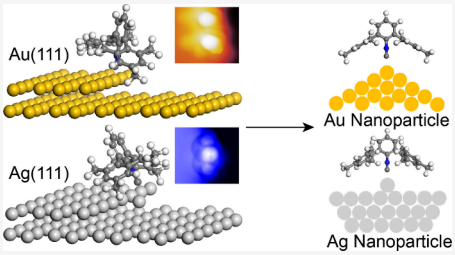

KEYWORDS: *ligand−nanoparticle interfaces, m-terphenyl isocyanide ligands, Au and Ag nanoparticles, surface-enhanced Raman spectroscopy, scanning tunneling microscopy*

Interfacial interaction between molecular ligands and metal surfaces is critical in shaping the chemical and physical properties of both the adsorbates and adsorbents.[1,2] It has been effectively employed as a key tool to engineer materials or structures with specific functions.[3,4] In nanoscience and nanotechnology, the importance of ligand−surface interaction is further amplified due to the high surface-to-volume ratio of the nanoparticles (NPs) and the frequent need for capping ligands in their preparation.[5,6] Research has demonstrated that even a minor modification in the capping ligands' structure or their surface coverage can significantly influence the NPs' properties.[7,8] Additionally, even the same ligand often interacts with different nanomaterials uniquely, due to the variation in ligand−surface interactions.[9−11] Consequently, the ability to precisely characterize and control these interfaces is highly desirable and offers a promising route toward the on-demand functionalization of nanostructures.

Metal NPs exhibit unique electronic,[12] optical,[13] and catalytic[14] properties, making them valuable in applications for sensing,[15] bioimaging,[16] drug delivery,[17] and heterogeneous catalysis.[18] The shape, size, and stability of these NPs are usually governed by capping ligands that adsorb to the metal surface during synthesis[19] or after postsynthetic ligand exchange,[20] leading to a strong dependence of NP properties on metal−ligand interactions. Surface-enhanced Raman spectroscopy (SERS),[21,22] infrared (IR) spectroscopy,[23,24] surface-enhanced infrared absorption (SEIRA) spectroscopy,[25,26] and nuclear magnetic resonance (NMR) spectroscopy[27,28] have provided crucial insights into the surface adsorption, coverage, and composition of these ligands. However, these ensemble-level techniques often face challenges such as signal convolution with matrix (as with NMR spectroscopy) or averaging of the spatially inhomogeneous signals (as with SERS, IR, and SEIRA spectroscopy), which can obscure data interpretation and complicate the understanding behind the nature of ligand−surface interactions at the sub-NP scale. These limitations highlight the need for molecular-scale characterization to achieve a more detailed understanding of nanoscale ligand binding to metal surfaces. Although attempts have been made to probe the ligand−NP interfaces with advanced microscopies such as scanning tunneling microscopy (STM),[29,30] atomic force microscopy,[31,32] and transmission electron microscopy,[33,34] progress in gaining single-molecule-

Received: November 20, 2024
Revised: January 13, 2025
Accepted: January 21, 2025
Published: January 23, 2025

https://doi.org/10.1021/acs.nanolett.4c05885
Nano Lett. 2025, 25, 2027−2033

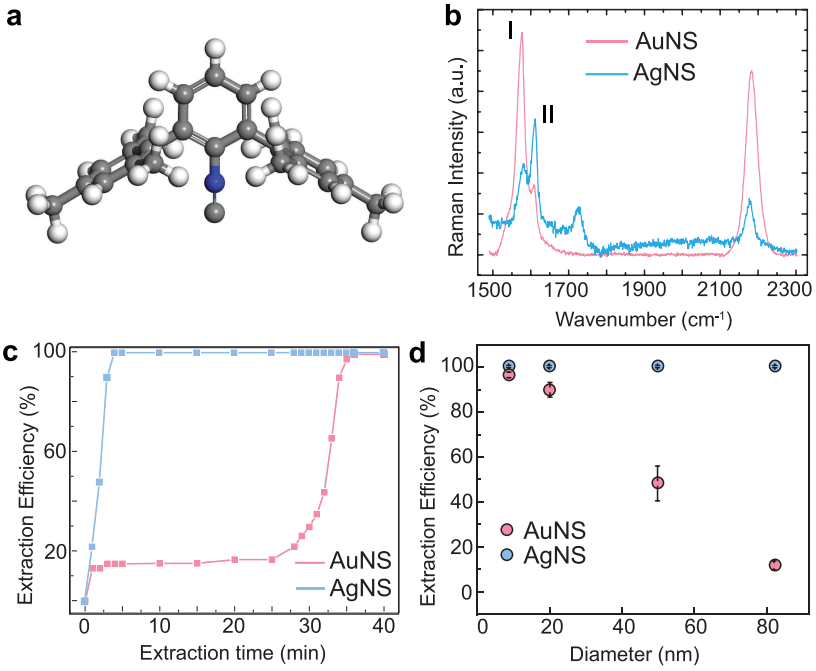

Figure 1. Solution-phase measurements reveal distinct binding behaviors of $CNAr^{Mes2}$ to AuNSs and AgNSs. (**a**) Molecular structure of $CNAr^{Mes2}$. C, H, and N atoms are shown in gray, white, and blue, respectively. (**b**) SERS spectra for AuNSs and AgNSs after LEPT with $CNAr^{Mes2}$. (**c**) Plot of the extraction efficiencies of 50 nm AuNSs and AgNSs extracted with $CNAr^{Mes2}$ in chloroform with respect to the extraction time. (**d**) Plot comparing the extraction efficiencies for AuNSs vs AgNSs of varied sizes.

level information on the ligand adsorption is limited due to the complexity of these interfaces.

m-Terphenyl isocyanides are a class of ligands known for their strong metal binding ability and distinct steric profile.[35,36] These ligands feature an aryl isocyanide (i.e., CNAr; Ar = aryl) metal-binding group whose binding to the metal surface is influenced by the steric interaction between the two additional mutually meta-positioned arenes and the metal surface. Due to this steric effect, we have previously demonstrated that the *m*-terphenyl isocyanide shown in Figure 1a, $CNAr^{Mes2}$ (Ar^{Mes2} = 2,6-(2,4,6-$Me_3C_6H_2$)$_2C_6H_3$),[35,37] readily binds to Au nanospheres (AuNSs) with diameters between 5 and 50 nm but shows minimal binding to larger NPs with lower nanocurvature.[38] Given this distinct threshold for curvature to ligand binding, we report here that $CNAr^{Mes2}$ binds indiscriminately to Ag nanospheres (AgNSs) of all sizes. This macroscopic contrast between Au and Ag NPs is a reflection of the unique properties, topologies, and adsorption profiles of metal surfaces of differing composition, reminiscent of the observed but yet not fully understood different interactions between N-heterocyclic carbenes with Au and Ag NPs.[10] Accordingly, to provide a molecular-scale understanding of these discrepancies, we performed microscopic investigations using an STM on $CNAr^{Mes2}$ adsorbed on Au(111) and Ag(111) surfaces. The results correlate the differences in ligand−NP interactions with the distinct adsorption structures of $CNAr^{Mes2}$ on Au and Ag surfaces. Together with first-principles electronic structure calculations, which elucidate the atomic binding morphology, these findings enable a clear and coherent picture of how $CNAr^{Mes2}$ interacts differently with Au and Ag surfaces at the molecular level.

To compare the binding behaviors of $CNAr^{Mes2}$ on AuNSs and AgNSs, we first performed ligand exchange in solution via phase transfer (LEPT) of citrate-stabilized pseudospherical AuNSs (56 ± 6 nm in diameter) and AgNSs (50 ± 4 nm in diameter) (Figure S1c) with $CNAr^{Mes2}$ between immiscible aqueous and chloroform phases (see the Supporting Information for details). LEPT reveals the tendency of $CNAr^{Mes2}$ to bind to AuNSs/AgNSs. Binding of $CNAr^{Mes2}$ to AuNSs/AgNSs was confirmed through the ν(CN) stretching vibration of isocyanide at ∼2180 cm^{-1} with SERS, a characteristic fingerprint of the metal-bound isocyanide (Figure 1b).[21,22,39−43] Notably, the relative intensity between the other two vibrational modes (denoted as I and II in Figure 1b) of $CNAr^{Mes2}$ differs significantly between AuNSs and AgNSs, suggesting variation of the SERS enhancement factor due to the different molecular adsorption geometries with respect to the NP surface.[43,44] LEPT efficiency was determined based on raffinate optical density obtained from extinction measurements (Figure S2 and section 1.4 in the Supporting Information). Figure 1c presents LEPT efficiencies of the 50 nm AuNSs and AgNSs with respect to exchange time, showing sigmoidal behavior for AuNSs that gradually increases before plateauing. This finding is consistent with previous observations that the steric interaction between $CNAr^{Mes2}$ and Au surfaces leads to a size selectivity of NPs.[38] In contrast, AgNSs are completely transported to chloroform within just 5 min. To further understand this difference in the binding of $CNAr^{Mes2}$ to Au versus Ag, we measured the LEPT efficiencies for AuNSs and AgNSs with varying diameters. Unlike AuNSs, whose extraction efficiency decreases with the diameter, AgNSs exhibit relatively high extraction efficiencies for all sizes, indicating indiscriminate binding of $CNAr^{Mes2}$ to the Ag surface (Figure 1d). This large difference in LEPT efficiency indicates that $CNAr^{Mes2}$ binds more favorably to Ag than to Au NP surfaces, potentially via a different binding mechanism, given the rapid ligand exchange kinetics.

To understand the difference between the ligation of AuNSs/AgNSs with $CNAr^{Mes2}$, we used STM to directly image the adsorption structure of $CNAr^{Mes2}$ on Au(111) and

https://doi.org/10.1021/acs.nanolett.4c05885
Nano Lett. 2025, 25, 2027−2033

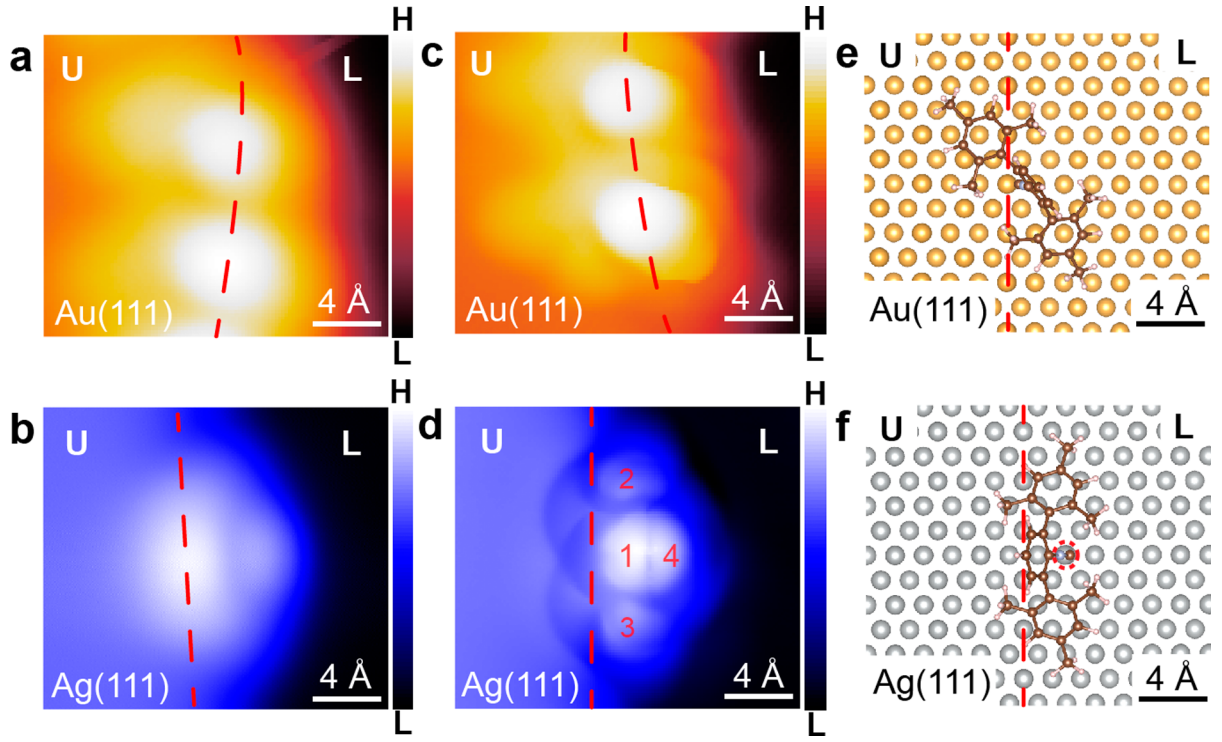

Figure 2. Distinct binding of $CNAr^{Mes2}$ to Au(111) and Ag(111). Conventional (**a, b**) and structure-resolved (**c, d**) STM images of $CNAr^{Mes2}$ at the step edge on Au(111) (a, c) and Ag(111) (b, d). (**e, f**) The top view of DFT-calculated adsorption geometries of $CNAr^{Mes2}$ at the step edge on Au(111) (e) and Ag(111) (f). The Ag adatom in (f) is highlighted by a red dashed circle. Step edges are indicated by red dashed lines. Upper (U) and lower (L) surface atomic layers are labeled for clarity. Note that (a, c) display two $CNAr^{Mes2}$ straddling the Au(111) step edge side by side while (e) simulates an individual molecule on Au(111) but still captures the critical straddling feature. Imaging parameters were −800 mV, 50 pA (a); −1 V, 20 pA (b); −565 mV, 100 pA (c); and −60 mV, 100 pA (d).

Ag(111) surfaces since the (111) facets are commonly used to represent the surfaces of Au and AgNPs that the ligands bind to.[45−51] Sample preparation procedures were previously described[52] and are detailed in section 1.5 of the Supporting Information. The intactness and chemisorption of $CNAr^{Mes2}$ on Au(111)[52] and Ag(111) (Figure S4 and section 3.1 in the Supporting Information) are corroborated by the molecular vibrational modes revealed with STM-inelastic electron tunneling spectroscopy (STM-IETS).[53,54] Figure 2a shows two $CNAr^{Mes2}$ positioned side by side, straddling a step edge on Au(111) (also in Figure S5a,b). This adsorption structure is consistent with our previous report indicating that $CNAr^{Mes2}$ energetically favors the convex sites on Au(111) due to the minimum steric interference from the vicinal Au surface atoms.[52] In contrast, $CNAr^{Mes2}$ also tends to populate the step edges on Ag(111) (Figure S5c,d); its appearance (Figure 2b) is significantly different from that on Au(111). First, on Au(111), individual $CNAr^{Mes2}$ appears as a single, intact entity. While on Ag(111), it appears as two overlapping compartments with a larger crescent feature on top of another smaller entity. Second, $CNAr^{Mes2}$ covers across the Au(111) step edge but, in contrast, displays an elongated contour along the step edge of Ag(111). Further differentiation between the adsorption behaviors of $CNAr^{Mes2}$ on Au(111) and Ag(111) was achieved in the high-resolution topographic images acquired using molecule-functionalized STM tips[55−57] (Figure 2c,d). Figure 2c clearly shows that $CNAr^{Mes2}$ spans across the Au(111) step edge, with the central aryl ring (highlighted by the bright white oval in Figure 2c) positioned directly above the step edge and two side mesityl groups situating on the upper and lower Au layers, respectively. In contrast, Figure 2d distinctly resolves the central (labeled with 1) and both of the side aryl rings (labeled with 2 and 3) of $CNAr^{Mes2}$, indicating that it resides in a geometry parallel to the Ag(111) step edge on top of another entity (labeled with 4), which we assigned as an Ag adatom. First-principles electronic structure calculations employing density functional theory (DFT) were used to determine the stable binding geometries of $CNAr^{Mes2}$ on these metal surfaces. We found that the straddling geometry of $CNAr^{Mes2}$ on Au(111), where the isocyanide group bonds to an Au atom at the step edge (Figure 2e and Figure S6), is most stable. Similarly, the DFT-predicted adsorption geometry on Ag(111) aligns well with our hypothesis. The $CNAr^{Mes2}$ directly adsorbs on an Ag adatom and tilts toward the upper Ag layer by 28.93° relative to the (111) direction (Figure 2f and Figure S7a), which agrees with the experimental observation in Figure 2d. This adatom adsorption effectively releases the steric pressure in the side aryl rings, leading to a more stable binding compared to that of the straddling geometry (Figure S7b).

The distinct adsorption structures of $CNAr^{Mes2}$ on Au(111) and Ag(111) correlate directly with the differences in the ligation behavior of $CNAr^{Mes2}$ on AuNSs and AgNSs. The STM image of $CNAr^{Mes2}$ on Ag(111) (Figure 2d) indicates the involvement of Ag adatoms for $CNAr^{Mes2}$ as a dominant binding mechanism. It is worth noting that migration and diffusion of Ag atoms at room temperature across the surface have been reported in many previous studies.[58−61] These active adatoms facilitate the rapid binding of $CNAr^{Mes2}$ to AgNSs of all sizes (Figure 1c,d), without requiring corners or edges to release the steric pressure, as observed for its binding to AuNSs.[38]

https://doi.org/10.1021/acs.nanolett.4c05885
Nano Lett. 2025, 25, 2027−2033

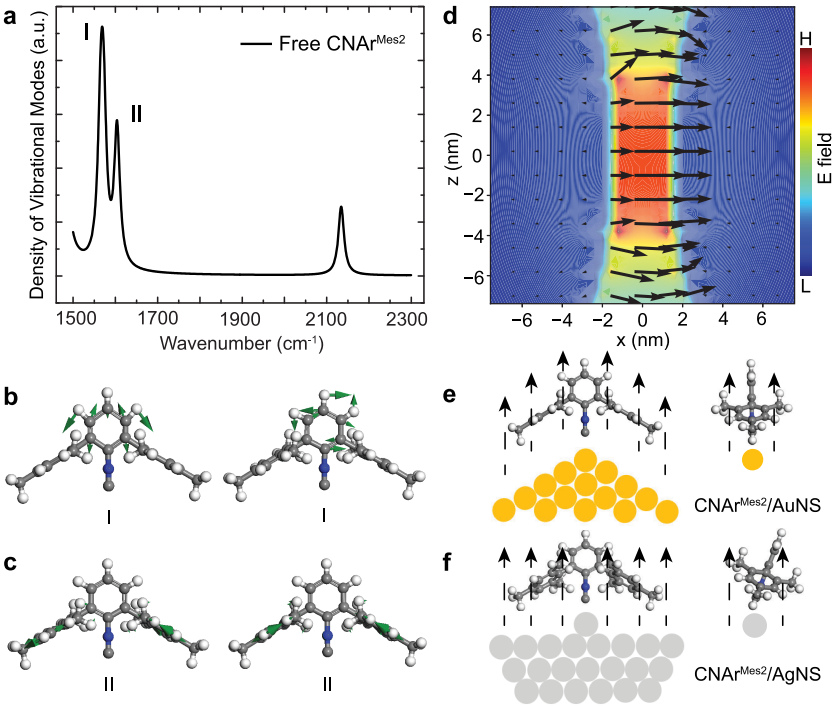

Figure 3. Deduced adsorption geometries of $CNAr^{Mes2}$ on AuNSs and AgNSs. (**a**) Calculated density of vibrational modes of free $CNAr^{Mes2}$. (**b, c**) Simulated nuclear motions of a free $CNAr^{Mes2}$ for modes I (b) and II (c). The green vectors indicate the direction and amplitude of the movements. (**d**) Simulated near field between two 50 nm AuNSs at the plasmon resonance with a wavelength of 543 nm. The black arrows show the field directions within the nanogap. (**e, f**) Schematic adsorption geometries of $CNAr^{Mes2}$ on AuNSs (e) and AgNSs (f). The right panels are side views of $CNAr^{Mes2}$ in each configuration. Black dashed arrows indicate the direction of the electric field in the SERS measurement.

The molecular-scale structural characterization also provides a clearer understanding of the variation in relative SERS signal intensity between modes I and II of $CNAr^{Mes2}$ bound to AuNSs and AgNSs (Figure 1b). According to our DFT simulations (Figure 3a), these two modes are identified as the deformation motions of the aryl rings. As shown in Figures 3b and 3c, mode I concerns the in-plane deformation of the central aryl ring (more discussion in Figure S8 and section 3.4 in the Supporting Information), while mode II involves the in-plane breathing motions of the two side aryl rings. In our SERS measurements, the NPs are closely spaced and sandwich the $CNAr^{Mes2}$ ligands within the nanogaps generated between neighboring NPs. The significantly enhanced electromagnetic fields within these gaps are predominantly polarized orthogonal to the surfaces of the metallic NPs (Figure 3d and section 2.3 in the Supporting Information), leading to the strongest enhancement of the Raman signals where molecular vibrations are aligned with the field direction.[43,44] Consequently, the stronger signal of mode I for $CNAr^{Mes2}$ bound to AuNSs (Figure 1b) indicates an adsorption configuration where the central aryl ring is perpendicular to the surface or parallel to the electric field (Figure 3e), consistent with the straddling adsorption of $CNAr^{Mes2}$ observed on Au(111) (Figure 2c). In contrast, the weakened mode I signal for $CNAr^{Mes2}$ bound to AgNSs (Figure 1b) implies a tilted central aryl ring (Figure 3f), which agrees with the observed geometry on Ag(111) (Figure 2d).

By integrating solution-phase analysis, molecular-scale characterization, and DFT calculations, we have developed a deeper understanding of the distinct ligation behavior of $CNAr^{Mes2}$ on AuNSs and AgNSs. On Au, $CNAr^{Mes2}$ straddles the edge and corner sites with the central aryl ring situated vertically on top of these convex surface sites (Figure 3e). On Ag, $CNAr^{Mes2}$ resides on an Ag adatom with the central aryl ring tilting toward the surface (Figure 3f). These two distinct binding mechanisms result in different behaviors during the solution-phase ligation process, including size selectivity for AuNSs versus rapid solvent extraction for AgNSs. We acknowledge that our STM characterization on the Au(111)/Ag(111) surface does not capture some critical information during the ligand binding to AuNSs/AgNSs, including multiple facets present on NPs, solution effects, other curved surface sites on NPs except for (111) step edges, etc., for constructing a more comprehensive picture of the ligand–NP interactions. Nonetheless, this study highlights the critical role of molecular-scale characterization in unraveling the complex interactions between metal NPs and organic ligands, offering valuable insights into the interfacial chemistry of metal NPs.

■ ASSOCIATED CONTENT

Supporting Information

The Supporting Information is available free of charge at https://pubs.acs.org/doi/10.1021/acs.nanolett.4c05885.

Experimental and computational methods, transmission electron microscope (TEM) images (Figure S1) and UV–vis spectra (Figure S2) of the $CNAr^{Mes2}$-bound AgNSs, ambient thermogravimetric analysis (TGA) plot of $CNAr^{Mes2}$ powder (Figure S3), STM-IETS spectrum of $CNAr^{Mes2}$ on Ag(111) (Figure S4), representative large-area STM images of $CNAr^{Mes2}$ on Au(111) and Ag(111) (Figure S5), and additional computational data of $CNAr^{Mes2}$ (Figures S6–S8) (PDF)

https://doi.org/10.1021/acs.nanolett.4c05885
Nano Lett. 2025, 25, 2027–2033

AUTHOR INFORMATION

Corresponding Authors

Andrea R. Tao − *Department of Chemistry and Biochemistry, University of California, San Diego, La Jolla, California 92093-0309, United States; Program in Materials Science and Engineering, University of California, San Diego, La Jolla, California 92093-0418, United States; Aiiso Yufeng Li Family Department of Chemical and Nano Engineering, University of California, San Diego, La Jolla, California 92093-0448, United States;* orcid.org/0000-0003-1857-8743; Email: atao@ucsd.edu

Shaowei Li − *Department of Chemistry and Biochemistry, University of California, San Diego, La Jolla, California 92093-0309, United States; Program in Materials Science and Engineering, University of California, San Diego, La Jolla, California 92093-0418, United States;* orcid.org/0000-0002-4627-626X; Email: shaoweili@ucsd.edu

Authors

Liya Bi − *Department of Chemistry and Biochemistry, University of California, San Diego, La Jolla, California 92093-0309, United States; Program in Materials Science and Engineering, University of California, San Diego, La Jolla, California 92093-0418, United States;* orcid.org/0009-0009-3041-2771

Yufei Wang − *Program in Materials Science and Engineering, University of California, San Diego, La Jolla, California 92093-0418, United States; Aiiso Yufeng Li Family Department of Chemical and Nano Engineering, University of California, San Diego, La Jolla, California 92093-0448, United States*

Zhe Wang − *Department of Physics and Astronomy, University of California, Irvine, California 92697-4575, United States; Institute of Fundamental and Frontier Sciences, University of Electronic Science and Technology of China, Chengdu 611731, China*

Alexandria Do − *Program in Materials Science and Engineering, University of California, San Diego, La Jolla, California 92093-0418, United States; Aiiso Yufeng Li Family Department of Chemical and Nano Engineering, University of California, San Diego, La Jolla, California 92093-0448, United States*

Alexander Fuqua − *Aiiso Yufeng Li Family Department of Chemical and Nano Engineering, University of California, San Diego, La Jolla, California 92093-0448, United States*

Krista P. Balto − *Department of Chemistry and Biochemistry, University of California, San Diego, La Jolla, California 92093-0309, United States;* orcid.org/0000-0001-7526-4885

Yanning Zhang − *Institute of Fundamental and Frontier Sciences, University of Electronic Science and Technology of China, Chengdu 611731, China;* orcid.org/0000-0002-3839-2965

Joshua S. Figueroa − *Department of Chemistry and Biochemistry, University of California, San Diego, La Jolla, California 92093-0309, United States; Program in Materials Science and Engineering, University of California, San Diego, La Jolla, California 92093-0418, United States;* orcid.org/0000-0003-2099-5984

Tod A. Pascal − *Program in Materials Science and Engineering, University of California, San Diego, La Jolla, California 92093-0418, United States; Aiiso Yufeng Li Family Department of Chemical and Nano Engineering, University of California, San Diego, La Jolla, California 92093-0448, United States;* orcid.org/0000-0003-2096-1143

Complete contact information is available at: https://pubs.acs.org/10.1021/acs.nanolett.4c05885

Author Contributions

#L.B., Y.W., Z.W.: These authors contributed equally to this work. The manuscript was written through contributions of all authors. All authors have given approval to the final version of the manuscript.

Notes

The authors declare no competing financial interest.

ACKNOWLEDGMENTS

The authors acknowledge the use of facilities and instrumentation supported by the United States National Science Foundation (NSF) through the UC San Diego Materials Research Science and Engineering Center (UCSD MRSEC) with Grant No. DMR-2011924. This work was primarily supported by the NSF under Grant CHE-2303936 (to Shaowei Li), DMR-2011924 (UCSD MRSEC), and the United States Department of Energy (DOE) under Grant DE-SC0025537 (to Andrea Tao and Shaowei Li). This work also used the Expanse supercomputer at the San Diego Supercomputing Center through allocation CSD799 from the Advanced Cyberinfrastructure Coordination Ecosystem: Services & Support (ACCESS) program, which is supported by NSF Grant No. 2138259, No. 2138286, No. 2138307, No. 2137603, and No. 2138296.

REFERENCES

(1) Turcheniuk, K.; Tarasevych, A. V.; Kukhar, V. P.; Boukherroub, R.; Szunerits, S. Recent advances in surface chemistry strategies for the fabrication of functional iron oxide based magnetic nanoparticles. *Nanoscale* **2013**, *5* (22), 10729−10752.

(2) Grassian, V. H. When Size Really Matters: Size-Dependent Properties and Surface Chemistry of Metal and Metal Oxide Nanoparticles in Gas and Liquid Phase Environments. *J. Phys. Chem. C* **2008**, *112* (47), 18303−18313.

(3) Daniel, M.-C.; Astruc, D. Gold Nanoparticles: Assembly, Supramolecular Chemistry, Quantum-Size-Related Properties, and Applications toward Biology, Catalysis, and Nanotechnology. *Chem. Rev.* **2004**, *104* (1), 293−346.

(4) Love, J. C.; Estroff, L. A.; Kriebel, J. K.; Nuzzo, R. G.; Whitesides, G. M. Self-Assembled Monolayers of Thiolates on Metals as a Form of Nanotechnology. *Chem. Rev.* **2005**, *105* (4), 1103−1170.

(5) Yin, Y.; Alivisatos, A. P. Colloidal nanocrystal synthesis and the organic-inorganic interface. *Nature* **2005**, *437* (7059), 664−670.

(6) Nam, J.-M.; Owen, J. S.; Talapin, D. V. The Ligand-Surface Interface and Its Influence on Nanoparticle Properties. *Acc. Chem. Res.* **2023**, *56* (17), 2265−2266.

(7) Samia, A. C. S.; Hyzer, K.; Schlueter, J. A.; Qin, C.-J.; Jiang, J. S.; Bader, S. D.; Lin, X.-M. Ligand Effect on the Growth and the Digestion of Co Nanocrystals. *J. Am. Chem. Soc.* **2005**, *127* (12), 4126−4127.

(8) Guan, H.; Harris, C.; Sun, S. Metal-Ligand Interactions and Their Roles in Controlling Nanoparticle Formation and Functions. *Acc. Chem. Res.* **2023**, *56* (12), 1591−1601.

(9) Samia, A. C. S.; Schlueter, J. A.; Jiang, J. S.; Bader, S. D.; Qin, C.-J.; Lin, X.-M. Effect of Ligand-Metal Interactions on the Growth of Transition-Metal and Alloy Nanoparticles. *Chem. Mater.* **2006**, *18* (22), 5203−5212.

(10) Ling, X.; Schaeffer, N.; Roland, S.; Pileni, M.-P. Nanocrystals: Why Do Silver and Gold N-Heterocyclic Carbene Precursors Behave Differently? *Langmuir* **2013**, *29* (41), 12647−12656.
(11) Lu, H.; Zhou, Z.; Prezhdo, O. V.; Brutchey, R. L. Exposing the Dynamics and Energetics of the N-Heterocyclic Carbene-Nanocrystal Interface. *J. Am. Chem. Soc.* **2016**, *138* (45), 14844−14847.
(12) Schön, G.; Simon, U. A fascinating new field in colloid science: small ligand-stabilized metal clusters and possible application in microelectronics. *Colloid Polym. Sci.* **1995**, *273* (2), 101−117.
(13) Kelly, K. L.; Coronado, E.; Zhao, L. L.; Schatz, G. C. The Optical Properties of Metal Nanoparticles: The Influence of Size, Shape, and Dielectric Environment. *J. Phys. Chem. B* **2003**, *107* (3), 668−677.
(14) Narayan, N.; Meiyazhagan, A.; Vajtai, R. Metal Nanoparticles as Green Catalysts. *Materials* **2019**, *12*, 3602.
(15) Hang, Y.; Boryczka, J.; Wu, N. Visible-light and near-infrared fluorescence and surface-enhanced Raman scattering point-of-care sensing and bio-imaging: a review. *Chem. Soc. Rev.* **2022**, *51* (1), 329−375.
(16) Kobayashi, K.; Wei, J.; Iida, R.; Ijiro, K.; Niikura, K. Surface engineering of nanoparticles for therapeutic applications. *Polym. J.* **2014**, *46* (8), 460−468.
(17) Verma, A.; Uzun, O.; Hu, Y.; Hu, Y.; Han, H.-S.; Watson, N.; Chen, S.; Irvine, D. J.; Stellacci, F. Surface-structure-regulated cell-membrane penetration by monolayer-protected nanoparticles. *Nat. Mater.* **2008**, *7* (7), 588−595.
(18) Peng, L.; You, M.; Wu, C.; Han, D.; Öçsoy, I.; Chen, T.; Chen, Z.; Tan, W. Reversible Phase Transfer of Nanoparticles Based on Photoswitchable Host-Guest Chemistry. *ACS Nano* **2014**, *8* (3), 2555−2561.
(19) Heuer-Jungemann, A.; Feliu, N.; Bakaimi, I.; Hamaly, M.; Alkilany, A.; Chakraborty, I.; Masood, A.; Casula, M. F.; Kostopoulou, A.; Oh, E.; Susumu, K.; Stewart, M. H.; Medintz, I. L.; Stratakis, E.; Parak, W. J.; Kanaras, A. G. The Role of Ligands in the Chemical Synthesis and Applications of Inorganic Nanoparticles. *Chem. Rev.* **2019**, *119* (8), 4819−4880.
(20) Merg, A. D.; Zhou, Y.; Smith, A. M.; Millstone, J. E.; Rosi, N. L. Ligand Exchange for Controlling the Surface Chemistry and Properties of Nanoparticle Superstructures. *ChemNanoMat* **2017**, *3* (10), 745−749.
(21) Zhang, Y.; Liu, J.; Ahn, J.; Xiao, T.-H.; Li, Z.-Y.; Qin, D. Observing the Overgrowth of a Second Metal on Silver Cubic Seeds in Solution by Surface-Enhanced Raman Scattering. *ACS Nano* **2017**, *11* (5), 5080−5086.
(22) Kim, K.; Kim, K. L.; Choi, J.-Y.; Lee, H. B.; Shin, K. S. Surface Enrichment of Ag Atoms in Au/Ag Alloy Nanoparticles Revealed by Surface-Enhanced Raman Scattering of 2,6-Dimethylphenyl Isocyanide. *J. Phys. Chem. C* **2010**, *114* (8), 3448−3453.
(23) Kim, H. S.; Lee, S. J.; Kim, N. H.; Yoon, J. K.; Park, H. K.; Kim, K. Adsorption Characteristics of 1,4-Phenylene Diisocyanide on Gold Nanoparticles: Infrared and Raman Spectroscopy Study. *Langmuir* **2003**, *19* (17), 6701−6710.
(24) Bian, H.; Li, J.; Chen, H.; Yuan, K.; Wen, X.; Li, Y.; Sun, Z.; Zheng, J. Molecular Conformations and Dynamics on Surfaces of Gold Nanoparticles Probed with Multiple-Mode Multiple-Dimensional Infrared Spectroscopy. *J. Phys. Chem. C* **2012**, *116* (14), 7913−7924.
(25) Kundu, J.; Le, F.; Nordlander, P.; Halas, N. J. Surface enhanced infrared absorption (SEIRA) spectroscopy on nanoshell aggregate substrates. *Chem. Phys. Lett.* **2008**, *452* (1), 115−119.
(26) Enders, D.; Rupp, S.; Küller, A.; Pucci, A. Surface enhanced infrared absorption on Au nanoparticle films deposited on SiO2/Si for optical biosensing: Detection of the antibody-antigen reaction. *Surf. Sci.* **2006**, *600* (23), L305−L308.
(27) Sharma, R.; Holland, G. P.; Solomon, V. C.; Zimmermann, H.; Schiffenhaus, S.; Amin, S. A.; Buttry, D. A.; Yarger, J. L. NMR Characterization of Ligand Binding and Exchange Dynamics in Triphenylphosphine-Capped Gold Nanoparticles. *J. Phys. Chem. C* **2009**, *113* (37), 16387−16393.
(28) Marbella, L. E.; Millstone, J. E. NMR Techniques for Noble Metal Nanoparticles. *Chem. Mater.* **2015**, *27* (8), 2721−2739.
(29) Jackson, A. M.; Myerson, J. W.; Stellacci, F. Spontaneous assembly of subnanometre-ordered domains in the ligand shell of monolayer-protected nanoparticles. *Nat. Mater.* **2004**, *3* (5), 330−336.
(30) Biscarini, F.; Ong, Q. K.; Albonetti, C.; Liscio, F.; Longobardi, M.; Mali, K. S.; Ciesielski, A.; Reguera, J.; Renner, C.; De Feyter, S.; Samorì, P.; Stellacci, F. Quantitative Analysis of Scanning Tunneling Microscopy Images of Mixed-Ligand-Functionalized Nanoparticles. *Langmuir* **2013**, *29* (45), 13723−13734.
(31) Lemoine, P.; Dooley, C.; Morelli, A.; Harrison, E.; Dixon, D. AFM study of organic ligand packing on gold for nanoparticle drug delivery applications. *Appl. Surf. Sci.* **2022**, *574*, 151386.
(32) Wang, X.; Wang, X.; Bai, X.; Yan, L.; Liu, T.; Wang, M.; Song, Y.; Hu, G.; Gu, Z.; Miao, Q.; Chen, C. Nanoparticle Ligand Exchange and Its Effects at the Nanoparticle-Cell Membrane Interface. *Nano Lett.* **2019**, *19* (1), 8−18.
(33) Pedrazo-Tardajos, A.; Claes, N.; Wang, D.; Sánchez-Iglesias, A.; Nandi, P.; Jenkinson, K.; De Meyer, R.; Liz-Marzán, L. M.; Bals, S. Direct visualization of ligands on gold nanoparticles in a liquid environment. *Nat. Chem.* **2024**, *16* (8), 1278−1285.
(34) Sardar, R.; Shumaker-Parry, J. S. Spectroscopic and Microscopic Investigation of Gold Nanoparticle Formation: Ligand and Temperature Effects on Rate and Particle Size. *J. Am. Chem. Soc.* **2011**, *133* (21), 8179−8190.
(35) Fox, B. J.; Sun, Q. Y.; DiPasquale, A. G.; Fox, A. R.; Rheingold, A. L.; Figueroa, J. S. Solution Behavior and Structural Properties of Cu(I) Complexes Featuring m-Terphenyl Isocyanides. *Inorg. Chem.* **2008**, *47* (19), 9010−9020.
(36) Ditri, T. B.; Fox, B. J.; Moore, C. E.; Rheingold, A. L.; Figueroa, J. S. Effective Control of Ligation and Geometric Isomerism: Direct Comparison of Steric Properties Associated with Bis-mesityl and Bis-diisopropylphenyl m-Terphenyl Isocyanides. *Inorg. Chem.* **2009**, *48* (17), 8362−8375.
(37) Carpenter, A. E.; Mokhtarzadeh, C. C.; Ripatti, D. S.; Havrylyuk, I.; Kamezawa, R.; Moore, C. E.; Rheingold, A. L.; Figueroa, J. S. Comparative Measure of the Electronic Influence of Highly Substituted Aryl Isocyanides. *Inorg. Chem.* **2015**, *54* (6), 2936−2944.
(38) Wang, Y.; Chen, A. A.; Balto, K. P.; Xie, Y.; Figueroa, J. S.; Pascal, T. A.; Tao, A. R. Curvature-Selective Nanocrystal Surface Ligation Using Sterically-Encumbered Metal-Coordinating Ligands. *ACS Nano* **2022**, *16* (8), 12747−12754.
(39) Robertson, M. J.; Angelici, R. J. Adsorption of Aryl and Alkyl Isocyanides on Powdered Gold. *Langmuir* **1994**, *10* (5), 1488−1492.
(40) Henderson, J. I.; Feng, S.; Bein, T.; Kubiak, C. P. Adsorption of Diisocyanides on Gold. *Langmuir* **2000**, *16* (15), 6183−6187.
(41) Joo, S.-W.; Kim, W.-J.; Yun, W. S.; Hwang, S.; Choi, I. S. Binding of Aromatic Isocyanides on Gold Nanoparticle Surfaces Investigated by Surface-Enhanced Raman Scattering. *Appl. Spectrosc.* **2004**, *58* (2), 218−223.
(42) Wu, Y.; Qin, D. In Situ Atomic-Level Tracking of Heterogeneous Nucleation in Nanocrystal Growth with an Isocyanide Molecular Probe. *J. Am. Chem. Soc.* **2018**, *140* (26), 8340−8349.
(43) López-Tobar, E.; Hara, K.; Izquierdo-Lorenzo, I.; Sanchez-Cortes, S. Plasmonic Effects of Phenylenediisocyanides Linked at Interparticle Junctions of Metal Nanoparticles. *J. Phys. Chem. C* **2015**, *119* (1), 599−609.
(44) Zeng, Y.; Ananth, R.; Dill, T. J.; Rodarte, A.; Rozin, M. J.; Bradshaw, N.; Brown, E. R.; Tao, A. R. Metasurface-Enhanced Raman Spectroscopy (mSERS) for Oriented Molecular Sensing. *ACS Appl. Mater. Interfaces* **2022**, *14* (28), 32598−32607.
(45) Lin, Y.; Pan, G.-B.; Su, G.-J.; Fang, X.-H.; Wan, L.-J.; Bai, C.-L. Study of Citrate Adsorbed on the Au(111) Surface by Scanning Probe Microscopy. *Langmuir* **2003**, *19* (24), 10000−10003.
(46) Park, J.-W.; Shumaker-Parry, J. S. Strong Resistance of Citrate Anions on Metal Nanoparticles to Desorption under Thiol Functionalization. *ACS Nano* **2015**, *9* (2), 1665−1682.

https://doi.org/10.1021/acs.nanolett.4c05885
Nano Lett. 2025, 25, 2027−2033

(47) Kunze, J.; Burgess, I.; Nichols, R.; Buess-Herman, C.; Lipkowski, J. Electrochemical evaluation of citrate adsorption on Au(111) and the stability of citrate-reduced gold colloids. *J. Electroanal. Chem.* **2007**, *599* (2), 147−159.
(48) Park, J.-W.; Shumaker-Parry, J. S. Structural Study of Citrate Layers on Gold Nanoparticles: Role of Intermolecular Interactions in Stabilizing Nanoparticles. *J. Am. Chem. Soc.* **2014**, *136* (5), 1907−1921.
(49) Ahuja, T.; Chaudhari, K.; Paramasivam, G.; Ragupathy, G.; Mohanty, J. S.; Pradeep, T. Toward Vibrational Tomography of Citrate on Dynamically Changing Individual Silver Nanoparticles. *J. Phys. Chem. C* **2021**, *125* (6), 3553−3566.
(50) Wright, L. B.; Rodger, P. M.; Walsh, T. R. Structure and Properties of Citrate Overlayers Adsorbed at the Aqueous Au(111) Interface. *Langmuir* **2014**, *30* (50), 15171−15180.
(51) Gisbert-González, J. M.; Cheuquepán, W.; Ferre-Vilaplana, A.; Herrero, E.; Feliu, J. M. Citrate adsorption on gold: Understanding the shaping mechanism of nanoparticles. *J. Electroanal. Chem.* **2020**, *875*, 114015.
(52) Bi, L.; Jamnuch, S.; Chen, A.; Do, A.; Balto, K. P.; Wang, Z.; Zhu, Q.; Wang, Y.; Zhang, Y.; Tao, A. R.; Pascal, T. A.; Figueroa, J. S.; Li, S. Molecular-Scale Visualization of Steric Effects of Ligand Binding to Reconstructed Au(111) Surfaces. *J. Am. Chem. Soc.* **2024**, *146* (17), 11764−11772.
(53) Stipe, B. C.; Rezaei, M. A.; Ho, W. Single-Molecule Vibrational Spectroscopy and Microscopy. *Science* **1998**, *280* (5370), 1732−1735.
(54) You, S.; Lü, J.-T.; Guo, J.; Jiang, Y. Recent advances in inelastic electron tunneling spectroscopy. *Advances in Physics: X* **2017**, *2* (3), 907−936.
(55) Li, S.; Czap, G.; Wang, H.; Wang, L.; Chen, S.; Yu, A.; Wu, R.; Ho, W. Bond-Selected Photodissociation of Single Molecules Adsorbed on Metal Surfaces. *Phys. Rev. Lett.* **2019**, *122* (7), 077401.
(56) Hahn, J. R.; Ho, W. Single Molecule Imaging and Vibrational Spectroscopy with a Chemically Modified Tip of a Scanning Tunneling Microscope. *Phys. Rev. Lett.* **2001**, *87* (19), 196102.
(57) Chiang, C.-l.; Xu, C.; Han, Z.; Ho, W. Real-space imaging of molecular structure and chemical bonding by single-molecule inelastic tunneling probe. *Science* **2014**, *344* (6186), 885−888.
(58) Gedara, B. S. A.; Muir, M.; Islam, A.; Liu, D.; Trenary, M. Room Temperature Migration of Ag Atoms to Cover Pd Islands on Ag(111). *J. Phys. Chem. C* **2021**, *125* (50), 27828−27836.
(59) Hong, J.-I.; Ding, Y.; Moon, K.-S.; Wong, C. P. Enhanced Diffusion of Silver Atoms on the Surface of Nanoparticles at Low Temperatures. *Journal of Electronic Packaging* **2013**, *135* (1), 011002.
(60) Pedemonte, L.; Tatarek, R.; Bracco, G. Surface self-diffusion at intermediate temperature: The Ag(110) case. *Phys. Rev. B* **2002**, *66* (4), 045414.
(61) Roşu, M. F.; Laurens, C. R.; Falepin, A.; James, M. A.; Langelaar, M. H.; Pleiter, F.; Rogojanu, O. C.; Niesen, L. Direct Observation of the Self-Diffusion Mechanism on the Ag(100) Surface. *Phys. Rev. Lett.* **1998**, *81* (21), 4680−4683.

https://doi.org/10.1021/acs.nanolett.4c05885
Nano Lett. 2025, 25, 2027−2033